OPEN ACCESS

Energy Conversion ARTICLE

The Innovation Energy

A low-stray-field thermomagnetic generator enabling high power density for low-grade waste heat recovery

Haodong Chen,[1] Mingze Liu,[1] Shengyun Jin,[1] Haowei Zhou,[2] Yili Cao,[2] Doudou Wang,[1] Haining Li,[1] Jiayi Sun,[1] Jincheng Wang,[1] Kaiming Qiao,[1] Adler G. Gamzatov,[3] Sergey V. Taskaev,[4] and Hu Zhang[1,*]

*Correspondence: zhanghu@ustb.edu.cn

Received: July 7, 2026; Accepted: October 7, 2026; Published Online: October 20, 2026; https://doi.org/10.59717/j.xinn-energy.2026.100192

© 2026 The Author(s). This is an open access article under the CC BY license (https://creativecommons.org/licenses/by/4.0/).

GRAPHICAL ABSTRACT



PUBLIC SUMMARY

- Topological thermomagnetic generator with compact closed magnetic circuit suppresses stray fields and reaches 65.2% magnetic flux utilization.
- Gd-based prototype cycles between 282–357 K, delivering ~0.16 V peak open-circuit voltage (0.051 V g^{-1}).
- Validated on Gd, Ho_2Fe_{17}/In, and $La(Fe,Si)_{13}H_y$/In at 290/330/335 K—material-adaptive across temperature windows.
- Six-unit series array scales near-linearly to ~0.8 V, demonstrating modular, scalable TMG architecture.

ARTICLE Energy Conversion

OPEN ACCESS

www.the-innovation.org/the-innovation-energy

A low-stray-field thermomagnetic generator enabling high power density for low-grade waste heat recovery

Haodong Chen,[1] Mingze Liu,[1] Shengyun Jin,[1] Haowei Zhou,[2] Yili Cao,[2] Doudou Wang,[1] Haining Li,[1] Jiayi Sun,[1] Jincheng Wang,[1] Kaiming Qiao,[1] Adler G. Gamzatov,[3] Sergey V. Taskaev,[4] and Hu Zhang[1,*]

[1]School of Materials Science and Engineering, University of Science and Technology Beijing, Beijing 100083, China

[2]Institute of Solid State Chemistry, Beijing Advanced Innovation Center for Materials Genome Engineering, University of Science and Technology Beijing, Beijing 100083, China

[3]Amirkhanov Institute of Physics, Dagestan Federal Research Centre of Russian Academy of Sciences, Makhachkala 367015, Russia

[4]Physics Faculty, Chelyabinsk State University, Chelyabinsk 454001, Russia

*Correspondence: zhanghu@ustb.edu.cn

Received: July 7, 2026; Accepted: October 7, 2026; Published Online: October 20, 2026; https://doi.org/10.59717/j.xinn-energy.2026.100192

© 2026 The Author(s). This is an open access article under the CC BY license (https://creativecommons.org/licenses/by/4.0/).

Citation: Chen H., Liu M., Jin S., et al. (2026). A low-stray-field thermomagnetic generator enabling high power density for low-grade waste heat recovery. *The Innovation Energy* **3**:100192.

Recovering electricity from low-grade waste heat remains a key challenge for distributed energy harvesting. Thermomagnetic generation (TMG) offers a solid-state approach by utilizing temperature-driven magnetization changes near the Curie temperature, but its performance is often limited by stray-field losses and inefficient magnetic-flux utilization. Here, we report a topological TMG with a compact closed magnetic circuit that suppresses stray fields and achieves a high magnetic flux utilization of 65.2%, much higher than those of representative topology-based TMGs (~50–53.9%). Under cyclic operation between 282 and 357 K, a Gd-based prototype generates an open-circuit peak voltage ($V_{oc\text{-}max}$) of ~0.16 V, corresponding to a voltage density of 0.051 V g^{-1}. The topology is further demonstrated using Gd, Ho_2Fe_{17}/In, and La(Fe, Si)$_{13}H_y$/In with transition temperatures of 290 K, 330 K, and 335 K, revealing distinct thermomagnetic switching responses and demonstrating compatibility with different operating temperature windows. A six-unit series array exhibits near-linear voltage scaling, reaching an $V_{oc\text{-}max}$ of ~0.8 V, demonstrating the modular scalability of the architecture. These results establish magnetic topology engineering as an effective route to improving magnetic flux utilization and electrical output while enabling material-adaptive and scalable thermomagnetic energy harvesting.

INTRODUCTION

The escalating global demand for sustainable energy has heightened the urgency of efficiently utilizing low-grade waste heat, which accounts for more than 60% of total industrial energy losses.[1,2] Recovering this abundant yet underexploited energy source is crucial for improving overall utilization efficiency and reducing carbon emissions.[3,4] Thermoelectric generators (TEGs) directly convert a temperature gradient into electricity through the Seebeck effect,[5,6] represent an established solid-state technology for waste heat recovery and generally suitable for heat sources below 600 K.[7,8] Nevertheless, achieving high conversion efficiency under small temperature gradients remains challenging because of the limited thermoelectric performance of available materials, while the relatively high fabrication cost and mechanical constraints of conventional modules can further hinder their widespread deployment.[9-11] Recent advances in thermoelectric materials and device engineering have substantially improved thermoelectric performance, interfacial reliability, and mechanical robustness, with high-performance devices also demonstrating effective harvesting of low-grade waste heat.[12-14]

Thermomagnetic generation (TMG), in contrast, offers a fundamentally different and complementary approach to low-grade waste heat harvesting by exploiting the pronounced temperature-dependent magnetization change of thermomagnetic materials (TMMs) near their magnetic transition temperatures.[15-18] This characteristic makes TMG particularly attractive for harvesting thermal fluctuations within a relatively narrow temperature window around the Curie temperature (T_C), including near-room-temperature heat sources when TMMs with appropriate T_C values are employed. Theoretical analyses indicate that TMGs can achieve higher theoretical conversion efficiencies than TEGs, Organic Rankine cycle (ORC) systems, and Stirling engines, particularly when the heat source temperature is below 400 K.[19] By converting the magnetization variation into electrical energy through magnetic flux modulation, TMG provides a vibration-free, potentially efficient, and scalable route for low-grade waste heat recovery.[20,21] Nevertheless, the practical advancement of TMG has been hindered by challenges in magnetic circuit design, efficient heat transfer management, enhancement of high-density power output, and cost reduction, all of which limit the translation of theoretical concepts into functional systems.

TMGs can generally be classified into passive and active types.[22] In passive TMGs, energy conversion occurs indirectly through mechanically induced motion, whereas active TMGs achieve direct thermal-to-electrical conversion driven by magnetization variation in TMMs. Passive TMGs typically couple a TMM with a cantilever beam, where the interplay among temperature gradients, magnetic forces, and elastic restoring forces induces self-sustained oscillations. Another representative configuration is the rotary TMG, in which TMMs undergo cyclic heating and cooling during rotation between regions of different temperatures. The resulting temperature-dependent magnetic forces generate a net torque to sustain rotary motion, which can subsequently be converted into electrical energy.[21,23,24] Such mechanical motion can be further converted into electricity through piezoelectric,[25,26] triboelectric,[27,28] pyroelectric[29] materials, or induction coils.[30-32] However, passive TMGs generally rely on a two-step conversion process (thermal-to-mechanical-to-electrical), which introduces additional energy dissipation and often results in relatively low output current and power.[27,30] In addition, repetitive mechanical motion may lead to material fatigue, frictional losses, and long-term reliability concerns. Moreover, the thermal contact between the TMMs and heat source in passive systems is often intermittent, which limits heat transfer efficiency and slows the thermal response. In contrast, active TMGs can theoretically offer higher conversion efficiencies than passive TMGs by directly utilizing the magnetization change of TMMs for electricity generation, thereby avoiding the additional thermal-to-mechanical energy conversion and associated losses in passive systems.[22,33,34] In particular, fluid-switching strategies provide direct convective heat transfer between the working fluid and TMMs, thereby enhancing thermal coupling and enabling rapid temperature modulation. The absence of mechanically moving solid components simplifies the device architecture and improves operational reliability. However, previously reported active TMGs still exhibit relatively low power outputs, primarily owing to insufficient magnetic flux variation within their magnetic circuits and the absence of systematic magnetic circuit optimization.[15,35-37]

Over the past decades, substantial efforts have been directed toward improving the output performance of TMG systems. Traditional TMGs typically adopt a magnetic circuit in which the TMM is placed inside the coil; thermal cycling modulates its magnetization and induces a corresponding change in magnetic flux. However, the resulting flux variation is usually small, yielding induced voltages on the order of only ~2 mV g^{-1}.[15,16,35] To overcome these inherent limits associated with single-loop flux modulation, researchers have explored topology-engineered magnetic circuits to amplify the usable magnetic-flux variation. A representative example is a pretzel-like magnetic-flux topology, which realized magnetic flux reversal and thus can achieve a maximum relative Carnot efficiency of 1.7×10^{-3} % at an operating frequency of 0.8 Hz and a temperature difference (ΔT) of 23 K.[38] However, its magnetic circuit enabled only partial utilization of the available flux, and the complex magnetic network required substantial material input and a nontrivial heat-

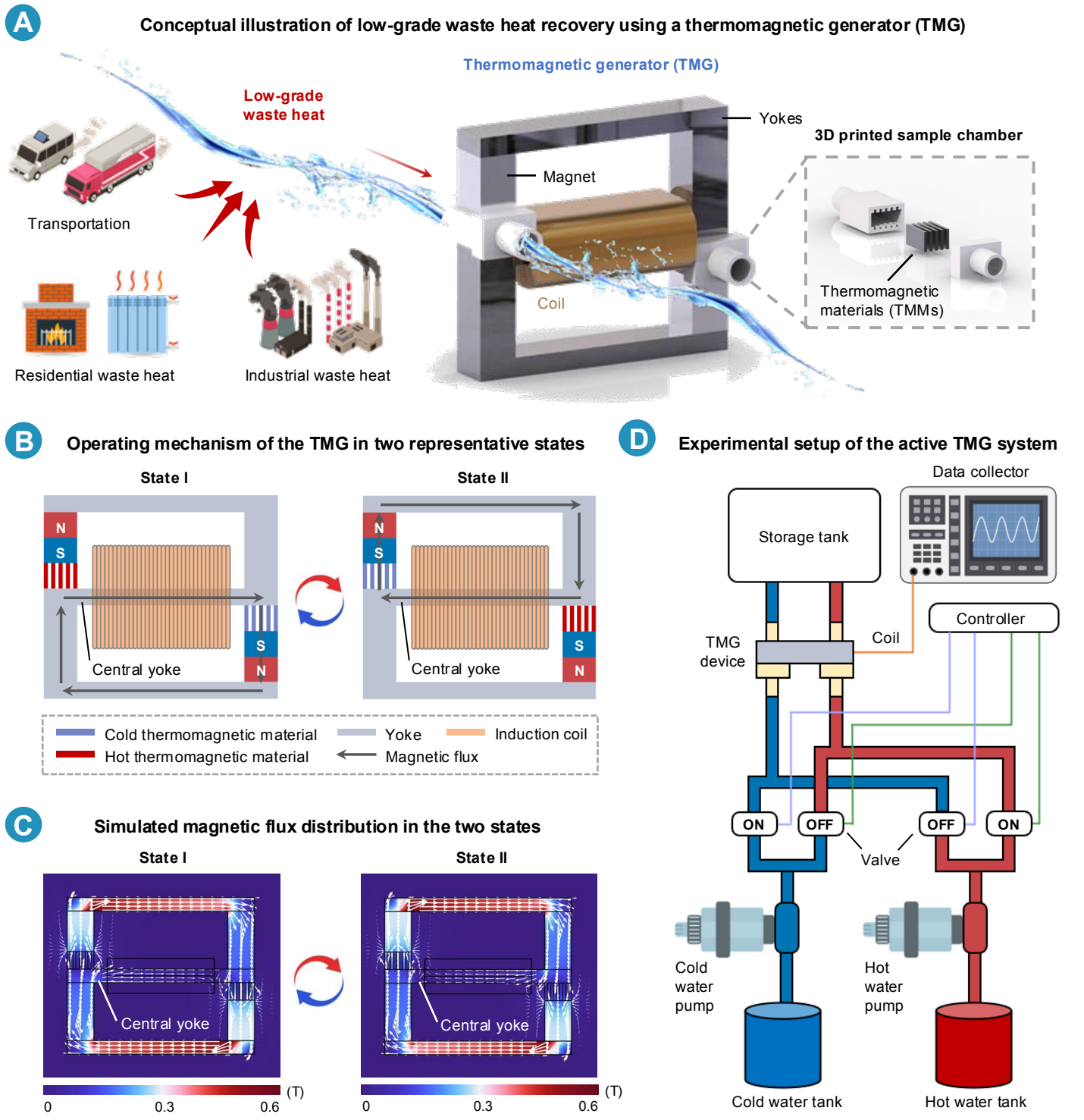


Figure 1. Working principle and system design of the thermomagnetic generator (TMG) (A) Conceptual illustration of low-grade waste heat recovery from various sources using a TMG. (B) Operating mechanism of the TMG in two representative states. State I: heating the samples on the left, cooling the samples on the right. State II: cooling the samples on the left, heating the samples on the right. (C) Finite-element simulations of the magnetic flux distribution in state I and state II, showing the flux transfer through the central yoke during thermal cycling. (D) Experimental setup of the active TMG system consisting of hot- and cold-water tanks, pumps, valves, a programmable controller, and a data collector, enabling automated thermal switching between the two states.

flow configuration, which complicated heat transfer and hindered scalability. Moreover, Liu et al.[34] developed another TMG incorporating magnetocaloric switches, which reduced the required material volume and delivered an induced voltage of 0.031 V g^{-1}. The switch-enabled flux routing improved controllability; however, the magnetic environment remained accompanied by appreciable stray fields, and the thermal response limited the attainable heat-transfer rate and overall conversion efficiency. Most recently, another topology-optimized TMG was developed by employing 120 g of Gd spheres and a ΔT of 40 K, achieving an output power of 9 mW.[39] This design demonstrated the potential of topology engineering to substantially enhance electrical performance. At the same time, such high-output configurations typically rely on relatively substantial magnetocaloric volumes and extended assemblies, which may, in some cases, lead to increased stray-field effects and influence their suitability for miniaturized or large-scale manufacturing scenarios.

Despite these notable advances, achieving simultaneously (i) large effective flux variation with minimal stray-field loss, (ii) rapid and uniform heat transfer across working materials, and (iii) a structurally simple, scalable architecture remains a key challenge. Addressing these unmet needs is essential for unlocking high-density, low-cost TMG suitable for practical low-grade waste heat recovery.

In this study, we developed a new topology TMG, as illustrated in Figure 1A. The proposed TMG designed for harvesting low-grade waste heat from diverse sources, such as solar thermal collectors, residential heating systems, transportation systems, and industrial processes, and converting it into electrical energy. In the present work, its TMG performance is experimentally demonstrated within a temperature range of 278–363 K, highlighting its potential as a thermal-to-electric conversion platform for distributed low-grade waste heat recovery. Compared with some previous active TMGs, which mainly focus on increasing magnetic flux variation through complex flux pathways, the present design not only realizes magnetic flux reversal, but also features a reduced magnetic stray field, strong scalability, and material minimization within a compact closed magnetic circuit, providing a simplified strategy for high-power-density TMG. Moreover, the device exhibits excellent thermal adaptability, and robust cyclic stability, maintaining consistent output performance over 83 thermal cycles. Benefiting from the optimized flux topology and efficient heat exchange structure, the TMG achieves a peak open-circuit voltage of 0.051 V g^{-1}, representing record-high values among reported active TMGs.[15,16,33–36,38–47] Furthermore, a six-unit TMG array was successfully constructed, exhibiting approximately linear scaling of the output voltage and power and delivering a total output power of ~160 μW. This experimentally demonstrated output falls within the power-consumption range relevant to selected low-power sensing and electronic applications. For future practical applications, the pulsed electrical output could be stored in a capacitor and delivered through power-management circuitry for intermittent operation.

MATERIALS AND METHODS

Preparation of the thermomagnetic materials

Commercial high-purity Gd (>99.99 wt.%, purity) was used directly as the primary thermomagnetic material without further alloying treatment. The Gd bulk was machined by precision wire cutting into ten plates with dimensions of 6.5×12×1 mm^3 for subsequent TMG assembly.

The Ho (99.9 wt.%, purity) and Fe (99.9 wt.%, purity) raw materials were melted in a high-vacuum arc furnace. Then, the samples were sealed in quartz tubes under a high-purity argon atmosphere, annealed at 1373 K for at least one week, and quenched in ice water to obtain high-quality Ho_2Fe_{17} single phase alloys. In addition, the $LaFe_{11.7}Si_{1.3}C_{0.2}$ (noted as La(Fe, Si)$_{13}$) was first prepared by induction melting under an Ar atmosphere and subsequently processed into ribbons by melt spinning. The ribbons were sealed in an evacuated quartz tube, annealed at 1373 K for 9 days, and then quenched in ice water. The annealed ribbons were pulverized into powders with particle sizes below 150 μm and subsequently hydrogenated at 623 K under a H_2 pressure of 0.2 MPa for 5 days to obtain the hydrogenated La(Fe, Si)$_{13}H_y$ alloy.

Because the Ho_2Fe_{17} and La(Fe, Si)$_{13}H_y$ alloys are intrinsically brittle and difficult to machine directly into thin plates, they were consolidated with ductile and thermally conductive In through hot pressing (Figure S1). Commercial high purity In powder (>99.99 wt.%, purity) with a particle size below 150 μm was used for composite consolidation. The thermomagnetic materials were first crushed into powders with particle sizes below 75 μm (300-mesh sieve) and mechanically mixed with In powder at a nominal In content of 20 wt.%. The mixtures were then loaded into a mold and hot-pressed in air at 413 K under 900 MPa for 15 min, producing dense 12×12×6 mm^3 composite blocks. At 413 K, In was sufficiently softened to promote redistribution among the thermomagnetic particles while avoiding excessive leakage from the mold. Silicone grease was applied to the mold/contact surface before pressing to limit direct exposure of In to air and thereby suppress oxidation during consolidation.

Characterization of the thermomagnetic materials

Magnetization and specific heat measurements were performed using a cryogen-free, cryocooler-based system (VersaLab, Quantum Design Inc.), and the thermal conductivity was measured by using the thermal transport option of the platform at a heating rate of ± 0.2 K min^{-1}. The microstructural features of the samples were characterized using a Zeiss EVO-18 scanning electron microscope (SEM), while their elemental composition was analyzed via energy-dispersive spectroscopy (EDS). The phase compositions and crystal structures of the composites were characterized by X-ray diffraction (XRD) using Cu Kα radiation. The XRD patterns of the Ho_2Fe_{17}/In and La(Fe, Si)$_{13}H_y$/In composites are shown in Figure S2. No obvious additional impurity phases were detected within the resolution of the XRD measurements, confirming that the primary thermomagnetic phases were retained after composite consolidation. The densities of the consolidated composites were measured using the Archimedes method, and the corresponding porosities were determined from the measured and theoretical densities. The consolidated Ho_2Fe_{17}/In and La(Fe, Si)$_{13}H_y$/In composites exhibited measured densities of 6.84 and 7.49 g cm^{-3}, respectively. SEM/EDS results (Figures S3 & S4) confirm a homogeneous distribution of the thermomagnetic and In phases throughout the composites, indicating effective consolidation and intimate interparticle contact. The hot-pressed blocks were subsequently machined by wire cutting into plates with the required thicknesses and hole configurations for TMG assembly. The influence of plate dimensions on the magnetic circuit was further evaluated (Figure S5), based on which a plate width of 6.5 mm was selected for the final device configuration.

Construction of the TMG device

The topology of the magnetic circuit is illustrated in Figure 1B. The circuit comprises three DT4C yokes (5×12×70 mm^3) as well as two side yokes (12×12×23.5 mm^3) connected by small permanent magnets (N52, 15×12×10 mm^3) and layered TMM plates (6.5×12×1 mm^3). The permanent magnets generate a stable magnetic field of approximately 0.5 T, while the closed-loop magnetic flux minimizes magnetic stray fields. A copper coil with 1600 turns is wound around the central yoke. The detailed structural parameters of the TMG are listed in Table S1. To enhance heat transfer rate, the TMM plates were fabricated into thin layers and assembled within a 3D-printed sample chamber. Hot and cold water were alternately circulated through the upper and lower TMMs, enabling the TMMs to open or close the magnetic circuit. A K-type thermocouple was employed to monitor the temperature variation of water within the chamber, while voltage and temperature data were recorded using a data acquisition system (RIGOL M300). Infrared images during TMG operation were captured with an infrared imager (HIKMICRO, HM-TPK20-3AQF/W) and processed using the HIKMICRO Analyzer software.

Finite element simulations

Numerical simulations were conducted using COMSOL Multiphysics (version 6.1). The Heat Transfer (HT) and Magnetic Fields (MF) modules were coupled to model the temperature evolution of the TMMs and the resulting induced voltage. The governing equations and corresponding boundary conditions adopted in the model are detailed in the Supplemental Note 1. The simulation outcomes were benchmarked against experimental measurements to assess and confirm the validity of the numerical model.

RESULTS

Design of topological magnetic circuit for the TMG

Figure 1B presents the topological structure and operating mechanism of the proposed TMG under two representative thermal states. The device consists of two symmetric magnetic circuit branches positioned above and below a central yoke, with a single induction coil wound around the middle yoke segment. Each branch contains several compact TMM plates serving as the thermomagnetic switch, and independent microchannels allow hot and cold fluids to be alternately delivered to the upper and lower branches during operation. In state I, when the hot water flows through the upper channel while cold water through the lower channel, the magnetic circuit in the upper branch is open, while the lower branch forms a closed loop due to the magnetic transition of the TMM. Consequently, the magnetic flux circulates clockwise within the lower circuit. In state II, upon reversing the temperature distribution, the lower circuit becomes open and the upper circuit closes, resulting in magnetic flux circulation in the upper loop. This alternating

switching between the two thermal states causes the magnetic flux within the induction coil wound around the central yoke to oscillate between positive and negative maxima. Thus, this bidirectional flux reversal effectively quadruples the induced power output. Moreover, unlike most traditional generators that use magnetic materials as the magnetic core, our configuration only uses a small amount of TMMs as the magnetic circuit switch. Therefore, it substantially reduces material consumption, fabrication cost, and assembly complexity. What is more, the use of smaller TMMs also minimizes magnetic stray fields that typically occur when flux passes through bulky yokes, thereby improving the induced voltage largely. These combined advantages enable the present TMG topology to achieve superior performance compared with previously reported configurations.

The finite-element simulations in Figure 1C illustrate the magnetic flux distribution of the TMG under representative two thermal states and clearly reveal the flux transfer between them. In state I, the magnetic flux is predominantly confined within the lower magnetic branch, while the upper branch remains magnetically open due to the paramagnetic state of the TMM. When the temperature field is reversed (state II), the active and inactive branches interchange, causing the magnetic flux in the central yoke to reverse direction. Beyond visualizing this bidirectional flux routing, the simulations also show that the proposed topology substantially suppresses stray magnetic fields. Owing to the compact closed-loop geometry and the use of only small TMM elements as switching units, the magnetic flux is tightly channeled into the intended circuit with minimal leakage into the surrounding air domain. This suppression of stray-field dispersion effectively increases the fraction of flux coupled through the central yoke, i.e., the effective magnetic flux variation ($\Delta\Phi$) that contributes to induction, rather than merely increasing the total flux circulating in the system. As a direct consequence, the present design achieves a nearly five-fold enhancement in $\Delta\Phi$ relative to the conventional single-loop configuration (Figure S6), establishing the central yoke as a critical amplifier of usable flux change and induced voltage. These simulation results validate the rationality of the magnetic circuit design and establish the theoretical foundation for efficient thermal-to-electrical conversion through cyclic thermal control.

Figure 1D further illustrates the operational sequence of the TMG under two thermal states. Hot and cold water are stored separately in insulated reservoirs, and both pumps operate continuously to maintain stable flow conditions. It should be noted that the pumps were used only to establish stable and reproducible thermal boundary conditions for laboratory characterization and were externally powered rather than driven by the TMG. In practical waste heat recovery, the TMG can be integrated with existing hot-fluid circulation or waste heat streams to minimize additional pumping requirements. The alternation between hot and cold water is regulated by four solenoid valves, which are sequentially controlled by a microcontroller to ensure precise timing. In state I, hot and cold water are simultaneously directed into the two sample chambers, inducing magnetic phase transitions that drive the left TMMs into paramagnetic (PM) state and the right TMMs into ferromagnetic (FM) state. When the flow direction is reversed (state II), the thermal conditions are swapped, converting the left TMMs into FM state and the right TMMs into PM state. This bidirectional thermal modulation reverses the magnetic flux in the central yoke, producing a substantial induced voltage in the surrounding coil.

Properties of the thermomagnetic materials

Figure 2A presents the temperature-dependent magnetization (M–T) curves of Gd measured under a magnetic field of 0.5 T during heating and cooling. The T_C, determined from the minimum of the dM/dT–T curve (Figure S7), is ~290 K. At low temperatures, Gd shows ferromagnetic ordering. Gd undergoes a pronounced FM–PM transition with increasing temperature, accompanied by a large magnetization change (ΔM) of 67 $Am^2\ kg^{-1}$ within the operating temperature window of 282–357 K. Meanwhile, the negligible thermal hysteresis between the heating and cooling curves indicates a reversible second-order magnetic transition, which is favorable for stable cyclic TMG operation. The large and reversible thermally induced magnetization variation provides substantial magnetic-flux modulation and is therefore directly beneficial to the electrical output of the TMG.

In addition to the magnetic transition, rapid heat transfer is essential because the induced voltage depends on the rate of magnetic flux variation during thermal switching. Figure 2B therefore summarizes the temperature-dependent specific heat (C_P), thermal conductivity (λ), and thermal diffusivity (a) of Gd. The C_P exhibits a moderate peak of 277 J kg^{-1} K^{-1} near T_C. This value is substantially lower than those of commonly used TMG materials, such as La(Fe, Si)$_{13}$-based alloys (~800 J kg^{-1} K^{-1})[35] and Ni-Mn-In Heusler alloys (652 J kg^{-1} K^{-1}).[36] A lower C_P is beneficial for TMG because it reduces the thermal energy required to drive temperature variation, thereby enabling faster temperature response under cyclic heating and cooling. Meanwhile, Gd exhibits a relatively high λ with an average value of about 10.1 W m^{-1} K^{-1} over the investigated temperature range. This value is significantly higher than those of many TMG materials, such as $Gd_5(Si, Ge)_4$ (~2.88 W m^{-1} K^{-1})[46] and $(Mn, Fe)_2(P, As)$ (~1.97 W m^{-1} K^{-1}).[40] The combination of low C_P and high λ results in enhanced thermal diffusivity, which can be calculted by $a = \lambda/(\rho C_P)$,[46] where ρ is the density of Gd. The resulting thermal diffusivity reaches 4.3–7.7×10^{-6} m^2 s^{-1} (inset of Figure 2B), facilitating rapid thermal equilibration during alternating heating and cooling. Taken together, the near room-temperature T_C, large reversible ΔM, favorable thermal transport, and good machinability make Gd well suited as the primary TMM for evaluating the proposed magnetic topology. Commercially available high-purity Gd can also be directly processed into thin plates without complex alloy synthesis or consolidation, facilitating its integration into the present TMG.

To further evaluate the material adaptability of the proposed topology, two additional TMMs with higher transition temperatures, Ho_2Fe_{17}/In and La(Fe, Si)$_{13}H_y$/In composites, were investigated. Their M–T curves under 0.5 T are shown in Figures 2C & D, respectively. Ho_2Fe_{17}/In exhibits a broad and reversible FM–PM transition centered at T_C = 330 K, with negligible thermal hysteresis (Figure S8). Its magnetization variation across the experimental thermal window is considerably smaller than that of Gd, indicating a relatively weaker magnetic-flux modulation. In contrast, La(Fe, Si)$_{13}H_y$/In exhibits a much sharper magnetic transition at T_C = 335 K across a narrow temperature interval, although a small separation between the heating and cooling curves is observed around the transition (Figure S9). The three TMMs thus provide distinct magnetic transition temperatures, with T_C values of 290, 330, and 335 K for Gd, Ho_2Fe_{17}/In, and La(Fe, Si)$_{13}H_y$/In, respectively. The selection of these three TMMs enables to examine how different T_C values influence thermomagnetic switching and the resulting voltage characteristics within the proposed topology. More importantly, their successful integration demonstrates that the topology of our TMG device is not restricted to a specific TMM, but can accommodate materials with different magnetic transition characteristics, providing flexibility for TMG operation over different temperature windows.

Realization and output characteristics of the TMG

The performance of the TMG was experimentally evaluated using Gd metal as the working material. Figure 3A shows the image of the assembled TMG device. Each 3D-printed sample chamber contained five Gd stacked plates (6.5×12×1 mm^3), separated by 1 mm gaps that allowed the heat exchange fluid to circulate through the interstitial channels. Small amount of Gd plates shortens the heating and cooling times, thereby improving the heat transfer rate. Together with permanent magnets, side yokes, and a central yoke wound with a 1600-turn copper coil, these components form a closed magnetic circuit. The top view of the experimental setup is displayed in Figure 3B. Alternating streams of hot and cold water were directed into the chambers to cyclically modulate the temperature of the Gd plates. The short flow channel length (12 mm) enabled rapid passage of the fluid, further enhancing the heat transfer rate. In addition, each magnetic branch employs only a very small amount of thin-plate Gd, which substantially shortens the thermal equilibration time and further increases the heat transfer rate during switching. The temperature-induced magnetization variation in the Gd plates dynamically alters the magnetic flux in the central yoke, which in turn generated an alternating voltage in the surrounding coil according to Faraday's law.

As shown in the real-time infrared image in Figures 3C & S10, during state I, the temperatures of the right and left inlet pipes for hot and cold water are approximately 67.1°C (340.1 K) and 31.8°C (304.8 K), respectively. When the hot and cold water flows are reversed (state II), the temperature distribution is correspondingly inverted. Figure 3D presents the simulated temperature

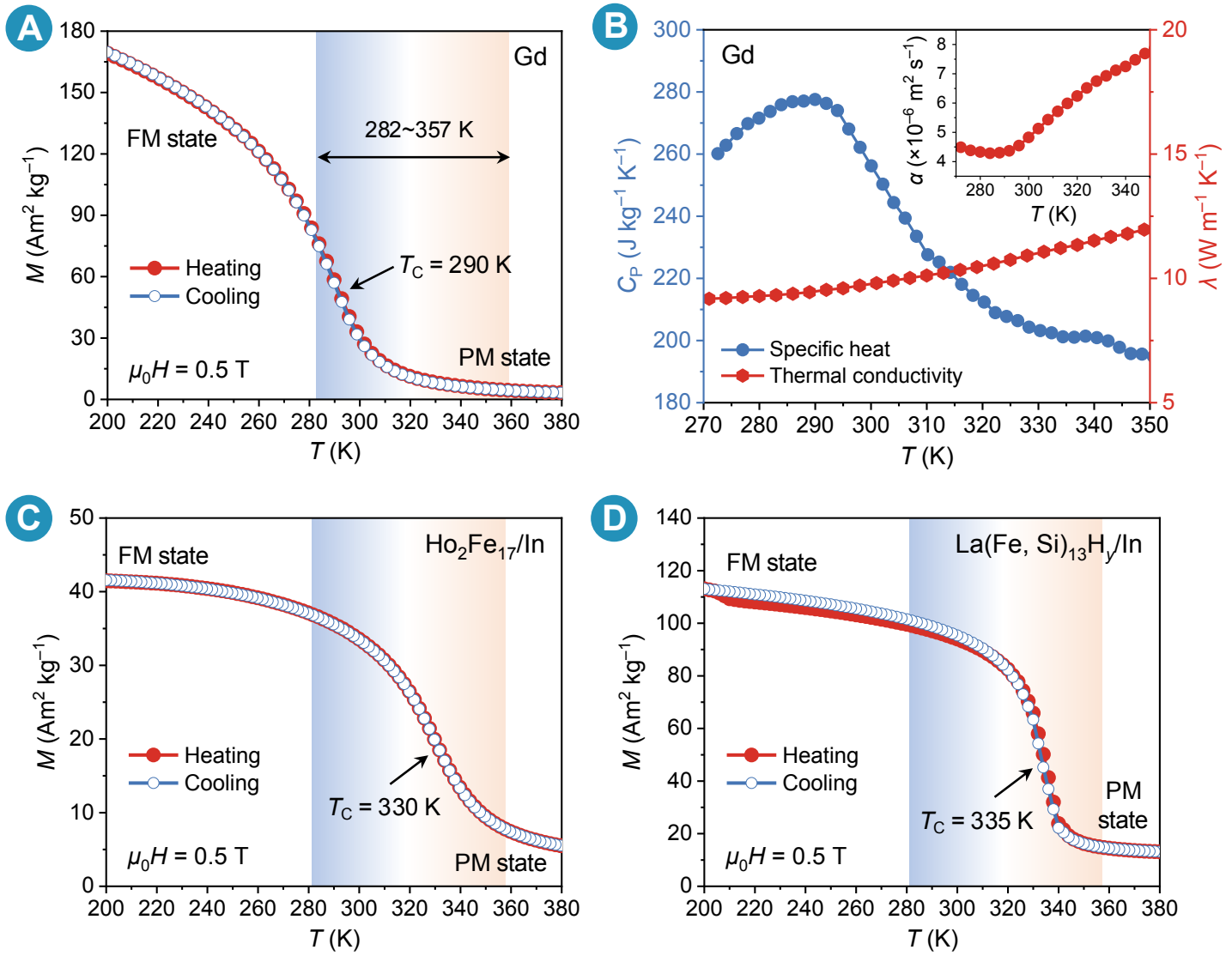


Figure 2. Magnetic and thermal properties of the thermomagnetic materials (A) The temperature-dependent magnetization (M–T) curves of Gd measured under a magnetic field of 0.5 T during heating and cooling. (B) Thermal properties of Gd, including specific heat (C_P) and thermal conductivity (λ). The inset shows the thermal diffusivity (α). (C,D) The M–T curves of Ho_2Fe_{17}/In (C) and $La(Fe, Si)_{13}H_y$/In (D) composites with different T_C values under a magnetic field of 0.5 T during heating and cooling.

evolution of the Gd plates in the left and right sample chambers, revealing that their temperatures vary synchronously but in opposite directions during each thermal cycle. Each heating–cooling cycle lasts 6 s. The temperature changes rapidly within the first ~1 s before gradually stabilizing at 282 K for the cold end and 357 K for the hot end (Figure S10). Notably, Figure S11 further shows that the entire Gd plates experience nearly complete heating or cooling within only ~0.5 s. This exceptionally short thermal response time highlights the high heat transfer rate enabled by the thin-plate geometry and compact flow channels, which in turn supports a larger dT/dt and contributes directly to the enhancement of induced voltage and output performance. These steady-state temperatures closely match the infrared measurements, confirming the periodic thermal cycling and efficient heat exchange between the fluid channels and the Gd plates.

Based on the Faraday's law, the induced voltage (V) generated by a thermomagnetic generator can be expressed as:[16,22,48]

$$V = -NS\frac{dB}{dt} \quad (1)$$

where N is the number of the coil turns, S is the cross-sectional area of the coil, and dB/dt represents the rate of change of the magnetic flux density. For a given device geometry, the term NS is fixed, meaning that the output voltage scales directly with the rate of magnetic-field change dB/dt. Because the magnetic field in the circuit can be expressed as $B = \mu_0 (H + M)$, the voltage ultimately depends on how rapidly the material magnetization evolves during thermal cycling. This temporal variation can be written as $dM/dt = (dM/dT)(dT/dt)$, indicating that both the sharpness of the magnetization transition near T_C and the speed at which the temperature of the TMM is modulated play central roles. Consequently, high-performance TMGs must simultaneously ensure a steep magnetization gradient and fast thermal switching to maximize the effective dM/dt and hence the induced voltage.

Figure 3E shows the experimentally measured and simulated open-circuit voltage (V_{oc}) of the TMG. When the left TMM is heated and the right TMM is cooled, a positive open-circuit voltage peak ($V_{oc\text{-}max}$) of ~0.16 V is observed at 0.04 s, followed by a small peak of ~0.013 V at ~0.95 s. These alternating large and small peaks persist throughout the cycle. States I and II are alternated every 3 s, corresponding to a thermal-state switching frequency of 0.33 Hz and a complete AC-cycle frequency of 0.167 Hz. Notably, the $V_{oc\text{-}max}$ is generated immediately after thermal switching rather than after thermal equilibrium is reached. Detailed waveform analysis (Figure S12) yields the full widths at half maximum (FWHMs) of ~0.066 s and ~0.089 s and continuous voltage-output durations of ~0.26 s and ~0.23 s for states I and II, confirming the highly transient nature of the thermomagnetic electrical output. The simulated results reproduce this trend, yielding large and small voltage peaks of 0.163 V and 0.025 V, respectively, which agree well with experimental

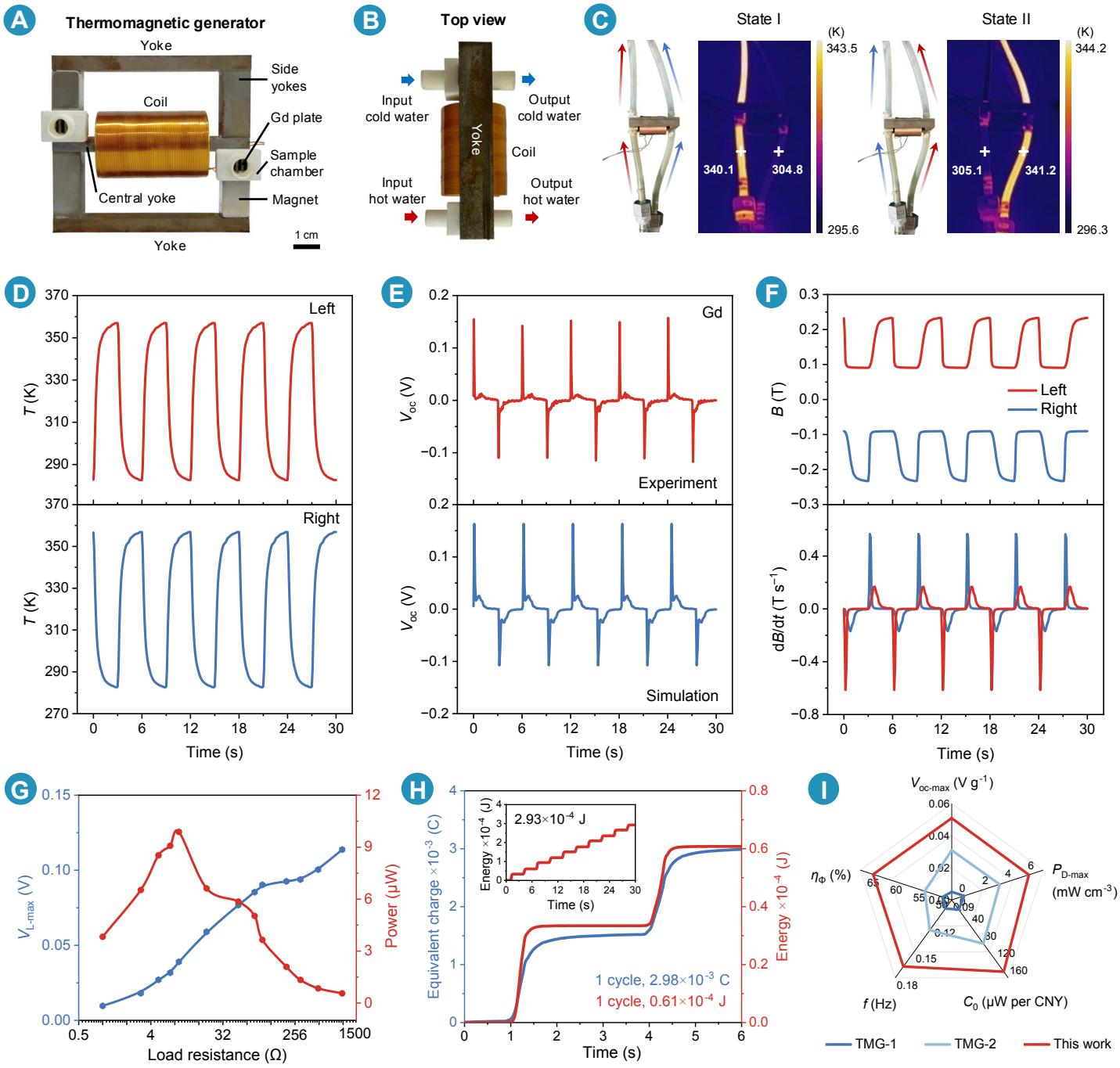


Figure 3. Device structure and performance characterization of the active TMG (A) Photo of the assembled TMG, consisting of a central yoke, side yokes, coil, and TMMs enclosed in a 3D-printed sample chamber. (B) Top view of the experimental setup showing the hot and cold water flow channels that trigger the magnetization change of the TMMs. (C) Infrared images of the TMG during two states. (D) The simulated temperature curves of the left and right regions of the TMMs. (E) Experimental and simulated voltage curves of the TMG under cyclic heating and cooling. (F) Time-dependent magnetic flux density (B) and its rate of change (dB/dt) at the left and right positions. (G) Peak load voltage ($V_{L\text{-max}}$) and average load power as functions of external load resistance (R_L). (H) Calculated accumulated charge and energy output over time during one operation cycle. The inset shows the energy output over 5 cycles. (I) Comparison of key TMG metrics of the present TMG with reported active TMGs with topology design,[34,45] including peak open-circuit voltage ($V_{oc\text{-max}}$), maximum power density ($P_{D\text{-max}}$), cost index (C_0), cycling frequency (f), and magnetic flux utilization (η_Φ).

results and validate the accuracy of the simulation model. The minor discrepancies, particularly the smaller experimental secondary peak, are attributed to measurement uncertainties and imperfect thermal conduction during operation. Moreover, we replaced Gd with another second-order transition material, Ho_2Fe_{17} (T_C = 330 K), whose T_C lies near the midpoint of the operating temperature window. In this configuration, the secondary peak nearly vanishes, and the voltage response becomes dominated by a single sharp maximum (Figure S13). This behavior confirms that the presence or absence of the secondary peak is governed by the location of T_C within the working temperature span. More importantly, this cross-material consistency establishes a generalizable design principle: a closed-loop topology that minimizes stray-field loss and maximizes effective $\Delta\Phi$ can deliver strong induced voltages across TMMs with different transition temperatures, illustrating the broad applicability and tunability of the proposed TMG framework for diverse material platforms and operating temperature windows.

To further elucidate the origin of these voltage oscillations, the magnetic flux density (B) distribution of the TMMs was analyzed via finite-element simulations (Figure 3F). The magnetic flux on the left and right sides is oppositely directed, with the left side defined as negative and the right as positive. When the left TMMs are heated and the right TMMs are cooled, the magnitude of $|B|$ decreases on the left side while increasing on the right. Because the T_C = 290 K of Gd is closer to the T_{Cold} (282 K) compared to the T_{Hot} (357

K), the FM–PM transition during heating occurs earlier than the PM–FM transition during cooling. As a result, the two TMMs do not undergo magnetic transitions simultaneously, even though the flow direction of hot and cold water is switched at the same time. Consequently, the reduction of $|B|$ on the left side occurs at 0.05 s, while the increase on the right side occurs later, around 0.95 s.

Furthermore, as shown in Figure 3D, the temperature change rate dT/dt near T_C = 290 K of Gd during heating is consistently higher than that during cooling, resulting in a faster decrease of $|B|$ compared to its subsequent increase (Figure 3F). The corresponding dB/dt profile (bottom of Figure 3F) reveals alternating large and small peaks of 0.61 T s^{-1} and 0.17 T s^{-1}, respectively. The ratio between these peaks closely matches the ratio of simulated voltage amplitudes, confirming that the observed successive large and small voltage peaks originate from asynchronous magnetic transitions between the two TMMs, as predicted by Faraday's law.

To further evaluate the electrical output under practical loading conditions, the TMG was connected to a series of external load resistances (R_L), and the corresponding load voltage (V_L) and average output power (P_L) were measured (Figure 3G). As R_L increases, the peak load voltage ($V_{L\text{-max}}$) increases progressively, whereas the P_L first increases and then decreases, exhibiting a clear maximum at R_L = 9 Ω. At this optimal load, $V_{L\text{-max}}$ reaches 0.039 V, with a maximum output power ($P_{L\text{-max}}$) of 0.17 mW and an average output power of 9.88 μW, corresponding to maximum power density ($P_{DL\text{-max}}$) and average power density (P_{DL}) of 0.43 mW cm^{-3} and 25.34 μW cm^{-3}, respectively. These results experimentally establish the optimal load condition and quantify the electrical power that can be extracted by an external load.

Low stray magnetic field and high comprehensive TMG performance

The electrical output characteristics of the TMG were further evaluated by calculating the equivalent charge (q) and accumulated electrical energy (Q), as shown in Figure 3H. Both of the equivalent charge $q = \int_0^t \frac{V_L(t)}{R_L} dt$ and accumulated energy $Q = \int_0^t \frac{V_L(t)^2}{R_L} dt$ were derived from the measured V_L–t curve (Figure S14). As shown in Figure 3H, each thermal cycle produced a charge transfer of approximately 2.98×10^{-3} C. The accumulated electrical energy reaches 0.61×10^{-4} J per cycle and 2.93×10^{-4} J over 5 cycles. The inset reveals a staircase-like increase in accumulated energy with successive thermal cycles, confirming the high repeatability of the thermomagnetic conversion process. Each cycle contributes nearly identical charge increments, reflecting the excellent reversibility of the FM–PM transition and stable operation under alternating thermal conditions. The nearly linear accumulation demonstrates not only the efficient conversion of thermal energy into magnetic flux variation but also the low intrinsic losses within the closed magnetic circuit. The combination of highly reproducible charge generation and steady energy accumulation underscores the intrinsic stability and scalability of the proposed TMG architecture. Compared with previously reported active TMG systems,[16,33,35,46] the present device exhibits enhanced charge output and energy density, attributed to its optimized magnetic circuit configuration, thereby enabling more reliable heat-to-electricity conversion.

Figure 3I presents a comprehensive analysis of key performance metrics of the present TMG and previously reported active TMGs featuring topology-optimized designs. For clarity, TMG–1 denotes the pretzel-like magnetic-flux topology,[38,45] whereas TMG–2 refers to the device employing a magnetocaloric-switch architecture.[34] To ensure a fair comparison, all devices employed Gd as the working material. Benefiting from the rapid magnetic flux variation dB/dt, our TMG device achieves the highest $V_{oc\text{-max}}$ = 0.051 V g^{-1}, exceeding those of TMG–1 (0.005 V g^{-1}) and TMG–2 (0.031 V g^{-1}) by factors of 10.2 and 1.6, respectively. The maximum power density ($P_{D\text{-max}}$), representing the output power per unit volume of magnetic material, was calculated as $P_{D\text{-max}} = V_{max}^2/RV_0$, where V_0 is the sample volume. Our device attains a $P_{D\text{-max}}$ of 5.76 mW cm^{-3}, approximately 60 times higher than that of TMG–1 (0.096 mW cm^{-3}).

To assess the material cost-effectiveness of different TMG configurations, we defined a TMM cost index (C_0) as $C_0 = P_{D\text{-max}}/C_v$, where $P_{D\text{-max}}$ is the maximum volumetric power density and C_v is the volumetric cost of the TMM. Accordingly, cost index C_0 represents the maximum electrical output per unit cost of the TMM.[49] For a consistent comparison, the three topology-based TMGs considered here employ Gd as the working material. Using a Gd density of 7.9 g cm^{-3} and a raw-material price of 5 CNY g^{-1}, C_v is 39.5 CNY cm^{-3}. The resulting C_0 values are 2.43, 81.01, and 145.82 μW per CNY for TMG–1, TMG–2, and the present TMG, respectively. Thus, the present topology achieves the highest TMM cost-effectiveness among the three configurations, primarily owing to its high power density and reduced TMM requirement. Detailed definitions, parameters, and step-by-step calculations are shown in Supplemental Note 2. Separately, the total material/component cost of the present laboratory-scale prototype is estimated to be approximately 31.22 USD, including the major components considered in the cost analysis, such as the TMMs, permanent magnets, magnetic yokes, copper wire, and 3D-printed nylon chamber (detailed calculations are shown in Supplemental Note 3). This estimate represents a component-level cost rather than the complete manufacturing cost and excludes expenses associated with sample machining (e.g., wire cutting), transportation, coil-winding labor, mold/fixture fabrication, manual assembly, and other processing procedures. Further cost reductions may be achievable through material optimization, simplified fabrication, and batch manufacturing.

The energy conversion efficiency was evaluated following the method reported previously,[38] using the maximum electrical power P_{max} and the thermal energy supplied by the circulating fluid: $\eta_{exp} = P_{max}/\Delta T Q_f \rho_f c_f$, where Q_f is the volumetric flow rate, and ρ_f and c_f are the density and specific heat capacity of water, respectively. The cold-side and hot-side temperatures used for the calculation were 282 and 357 K, respectively, corresponding to an operating temperature span (ΔT) of 75 K. The experimental efficiency (η_{exp}) was further normalized by the corresponding Carnot efficiency to obtain the relative conversion efficiency (η_{rel}), yielding a value of 0.14×10^{-5}%. The relatively low efficiency primarily originates from the large thermal input associated with the broad operating temperature span (~75 K) and relatively long thermal cycle (~6 s), while only a small fraction of the supplied heat is effectively utilized by the TMMs. Therefore, reducing the operating temperature span and increasing the cycling frequency through improved fluid-circulation and thermal-management design provide important route in the future.

In addition, the cycling frequency (f) corresponding to the maximum voltage output serves as an indicator of the device's dynamic response. As shown in Figure 3I, our TMG reaches $V_{oc\text{-max}}$ at f = 0.167 Hz, outperforming reported topology-optimized TMGs (TMG–1: 0.1 Hz; TMG–2: 0.125 Hz). This rapid thermal–magnetic cycling arises from the synergistic optimization of the heat transfer pathways and magnetic circuit. The short flow channel structure promotes rapid and uniform heat exchange between the working fluid and Gd plates, enhancing the temperature change rate across the magnetic transition region. Simultaneously, the closed magnetic yoke minimizes magnetic reluctance and confines flux efficiently, ensuring strong and synchronized dB/dt with thermal modulation. These coupled thermal and magnetic optimizations enable rapid and stable FM–PM cycles, yielding high voltage output even at elevated cycling frequencies.

More importantly, Figure 3I also compares the magnetic flux utilization (η_Φ) of the TMGs. Assuming magnetic flux conservation, the magnetic flux change in the coil corresponds directly with the material's intrinsic flux change ($\Delta\Phi_{mat}$), the detailed calculations can be found in Supplemental Note 4. In our experiments the coil-linked flux change ($\Delta\Phi_{sim}$) reaches ~65.2% of this theoretical maximum ($\eta_\Phi = \Delta\Phi_{sim} / \Delta\Phi_{mat}$ = 65.2%), whereas TMG–1 and TMG–2 attain only ~53.9% and 50%, respectively. A higher η_Φ indicates more effective confinement and utilization of the available magnetic flux, and consequently reduced magnetic-flux leakage. Stated differently, the fraction of flux lost to leakage in our design is ~34.8%, significantly smaller than in the comparison devices. This improvement is significant because effective magnetization change experienced by the TMM directly determines the magnetic flux utilization, and even modest increases in flux confinement are difficult to achieve once the magnetic circuit approaches a closed-loop configuration. This improved flux utilization is the principal mechanism behind the device's enhanced electrical output: because the induced voltage scales with the time derivative of the coil-linked flux, $V \propto d\Phi/dt$, suppressing leakage directly increases $d\Phi/dt$ and hence V_{oc} and the extracted power.

Four structural and physical factors explain the strong suppression of stray

fields in the present topology: (1) The thermomagnetic material inventory is deliberately minimal (thin Gd plates used only as switching elements), so no large magnetized body forms outside the designed magnetic paths; this fundamentally reduces fringe-field sources. (2) Both magnetic branches are implemented as short, high-permeability paths: magnetic reluctance $R_{mag} = l/\mu A$ is therefore low (where l is the length of magnetic path, μ is the magnetic permeability of sample, A is the cross-sectional area), which funnels flux through the intended circuit and diminishes leakage through the surrounding air. (3) The central yoke geometry is optimized to concentrate flux (high effective μ and favorable cross-sectional area A), increasing flux confinement and further lowering the propensity for field lines to bulge into the air. (4) The circuit is effectively closed during each state (minimal unintended gaps), so air-gap reluctances, the primary channel for stray flux, are largely eliminated. Taken together these features raise the effective flux utilization, simulations reveal a clear reduction in stray magnetic field relative to earlier topology-optimized TMG architectures (Figure S15). In short, by combining minimal TMM volume, short/high-μ flux paths, an optimized central yoke and near-closed magnetic circuits, the design suppresses stray-field losses and converts a much larger fraction of the material's magnetization change into usable coil flux, the key physical reason for the observed jump in $d\Phi/dt$, induced voltage and power density. These results show that suppressing stray-field losses and accelerating heat transfer allow this topology to convert a substantially larger fraction of the material's intrinsic magnetization change into usable coil flux. Consequently, the present TMG achieves higher voltage, power density, and cycling speed than earlier architectures, establishing a scalable and efficient platform for practical low-grade waste-heat recovery.

Thermal adaptability and long-term cyclic stability

Figure 4A shows the simulated dependence of $V_{oc\text{-}max}$ on the cold source temperature (T_{Cold}) and hot source temperature (T_{Hot}) using COMSOL Multiphysics. The heat map clearly identifies an optimal operating region, where $V_{oc\text{-}max}$ reaches its maximum at ΔT = 65 K and T_{Cold} = 273 K. This result indicates that broadening the effective woking temperature range across the magnetic transition window is essential for enhancing voltage output. Furthermore, when ΔT is fixed at 65 K, V_{max} increases as the ΔT shifts from 298–363 K to 278–343 K. Given that $V \propto (dB/dT)(dT/dt)$, the maximum voltage is achieved when both dB/dT and dT/dt attain their highest values. Typically, the peak dB/dT occurs near the T_C = 290 K. As shown in Figure S16, the temperature corresponding to the maximum dT/dt decreases and gradually approaches T_C as the ΔT shifts downward, resulting in the increase of $V_{oc\text{-}max}$. Therefore, a large ΔT combined with the highest dT/dt near T_C is most favorable for achieving high TMG performance.

Figure 4B shows the measured $V_{oc\text{-}max}$ of the TMG as a function of the T_{Cold}, with corresponding V_{oc}–t curves provided in Figure S17. When T_{Cold} = 298 K, which is higher than the T_C, the magnetic transition of Gd hardly occurs, resulting in negligible voltage generation. As T_{Cold} decreases, the PM–FM transition of Gd is more completely triggered by the colder water, leading to a larger ΔB (Figure S18). Moreover, a lower T_{Cold} enhances the dT/dt. The combined increase in ΔB and dT/dt yields a higher dB/dt, thereby increasing $V_{oc\text{-}max}$ from 0.02 V at 298 K to 0.15 V at 278 K, and the power output rises from 1.2 μW to 39.1 μW (Figure S19).

Similarly, Figure 4C shows the effect of the hot source temperature on $V_{oc\text{-}max}$, with the measured V_{oc}–t curves shown in Figure S20. Although $V_{oc\text{-}max}$ increases with T_{Hot} from 313 K to 363 K, the increase rate is slower than that observed with decreasing T_{Cold}. As revealed in Figure S21, ΔB increases only marginally with T_{Hot} because T_{Hot} = 313 K already exceeds T_C, so that Gd is fully converted into the paramagnetic state and ΔB reaches a high level. Further elevating T_{Hot} produces only a minor reduction in magnetic flux, ΔB increases merely ~0.021 T as T_{Hot} rises from 313 K to 363 K. Consequently, the corresponding increase in $|dB/dt|$ is only 0.095 T s^{-1}, much smaller than the 0.47 T s^{-1} achieved when lowering T_{Cold} from 298 K to 278 K. As a result, $V_{oc\text{-}max}$ and power output increases gradually from 0.072 V and 22 μW at 313 K to 0.151 V and 39 μW at 363 K (Figure S22). Overall, these results demonstrate that lowering T_{Cold} or increasing T_{Hot} increases promotes complete magnetic transition across the sample volume, resulting in a higher ΔB and larger induced voltage. The strong agreement between experimental and simulated result validates the accuracy of the heat transfer model in capturing both the temperature field and the magnetic response of the Gd plates during cyclic operation.

Figure 4D further summarizes the dependence of the average output power (P_{ave}) on the temperature difference (ΔT) under two operating modes. When the T_{Cold} is fixed at 278 K and the T_{Hot} is increased, the P_{ave} increases monotonically with ΔT, rising from 22 μW at ΔT = 35 K to 39 μW at ΔT = 85 K. This behavior originates from the enhanced ΔM between the hot and cold states as the temperature span widens, which leads to a larger magnetic flux variation and thus higher electrical output. In contrast, when the T_{Hot} is fixed at 363 K and ΔT is tuned by varying the T_{Cold}, the P_{ave} remains relatively low at small ΔT and increases noticeably only when the T_{Cold} approaches the Curie transition region of Gd. This trend indicates that, besides the magnitude of ΔT, the absolute temperature window relative to the T_C plays a critical role in determining the TMG performance. Specifically, when the operating temperature range straddles the magnetic transition region, the magnetization change becomes more pronounced, resulting in enhanced output power. These results demonstrate that both increasing ΔT and properly positioning the operating temperatures around the magnetic transition region are essential for maximizing the TMG performance.

Figure 4E compares the normalized power density ($P_{D\text{-}max}/\Delta T$) of the present TMG with previously reported active TMGs. Normalizing the power density by ΔT enables a fair comparison by minimizing the influence of operating temperature span, thereby better reflecting the intrinsic effectiveness of device design and magnetic flux utilization. The results show that our device achieves a $P_{D\text{-}max}/\Delta T$ of 0.077 mW cm^{-3} K^{-1}, which is 64% higher than that of a TMG employing a magnetocaloric switch (0.047 mW cm^{-3} K^{-1}) and 133% higher than that of the pretzel-like topology design (0.033 mW cm^{-3} K^{-1}). Notably, the obtained value also exceeds those of most reported active TMGs by 2–3 orders of magnitude. The markedly improved normalized performance indicates that the enhanced output does not merely arise from a larger ΔT, but primarily from the optimized magnetic topology and more efficient flux variation achieved in the present device.

To evaluate the feasibility under near room-temperature cooling conditions, we further investigated a TMM with a higher T_C. A La(Fe, Si)$_{13}$H$_y$/In composite with T_C = 335 K was employed as the working material (as shown in Figure 2D), enabling the magnetic transition to occur within a temperature window closer to ambient conditions. Figure 4F shows the $V_{oc\text{-}max}$ as a function of the T_{Cold} for La(Fe, Si)$_{13}$H$_y$/In, with the measured V_{oc}–t curves shown in Figure S23. Stable and repeatable voltage outputs are obtained over a wide range of T_{Cold} from 278 K to 308 K. Although the output voltage gradually decreases with increasing T_{Cold}, pronounced voltage signals are still clearly observed even at T_{Cold} = 298 K and 308 K. Specifically, when the T_{Cold} increases from 278 K to 298 K, the voltage of the La(Fe, Si)$_{13}$H$_y$/In composite decreases only by 16% (from 0.086 V to 0.073 V), which is substantially smaller than the 87% reduction observed for Gd under the same condition (from 0.15 V to 0.02 V, Figure 4B). This result indicates that the magnetic transition of the La(Fe, Si)$_{13}$H$_y$/In remains effective under near room-temperature cooling conditions. The reduced performance observed for Gd at room temperature originates from the mismatch between its T_C and the operating temperature window, rather than from intrinsic limitations of the TMG architecture. Therefore, by selecting TMMs with appropriately tuned transition temperatures, the proposed TMG can maintain appreciable output under ambient cooling conditions. In practical applications, the low-grade waste heat sources can cover a broad temperature range, with heat sources around 300–370 K being particularly relevant to the conditions examined in this work. Therefore, higher-T_C TMMs can be employed when operation closer to or above room temperature is desired, and the effective operating window can be further extended by selecting TMMs with appropriate T_C.

Figure 4G presents the variation of $V_{oc\text{-}max}$ and average power (P_{ave}) as a function of cycle period for the TMG using Gd metal. The corresponding V_{oc}–t curves are provided in Figure S24. As the cycle period shortens from 12 s to 6 s, $V_{oc\text{-}max}$ remains nearly constant while P_{ave} increases markedly, indicating that the magnetic transition of Gd is not affected at this timescale. The higher operating frequency produces more frequent voltage peaks, thereby enhancing the average power output. Notably, the optimal cycle period of 6 s represents a meaningful improvement compared with previously reported fluid-

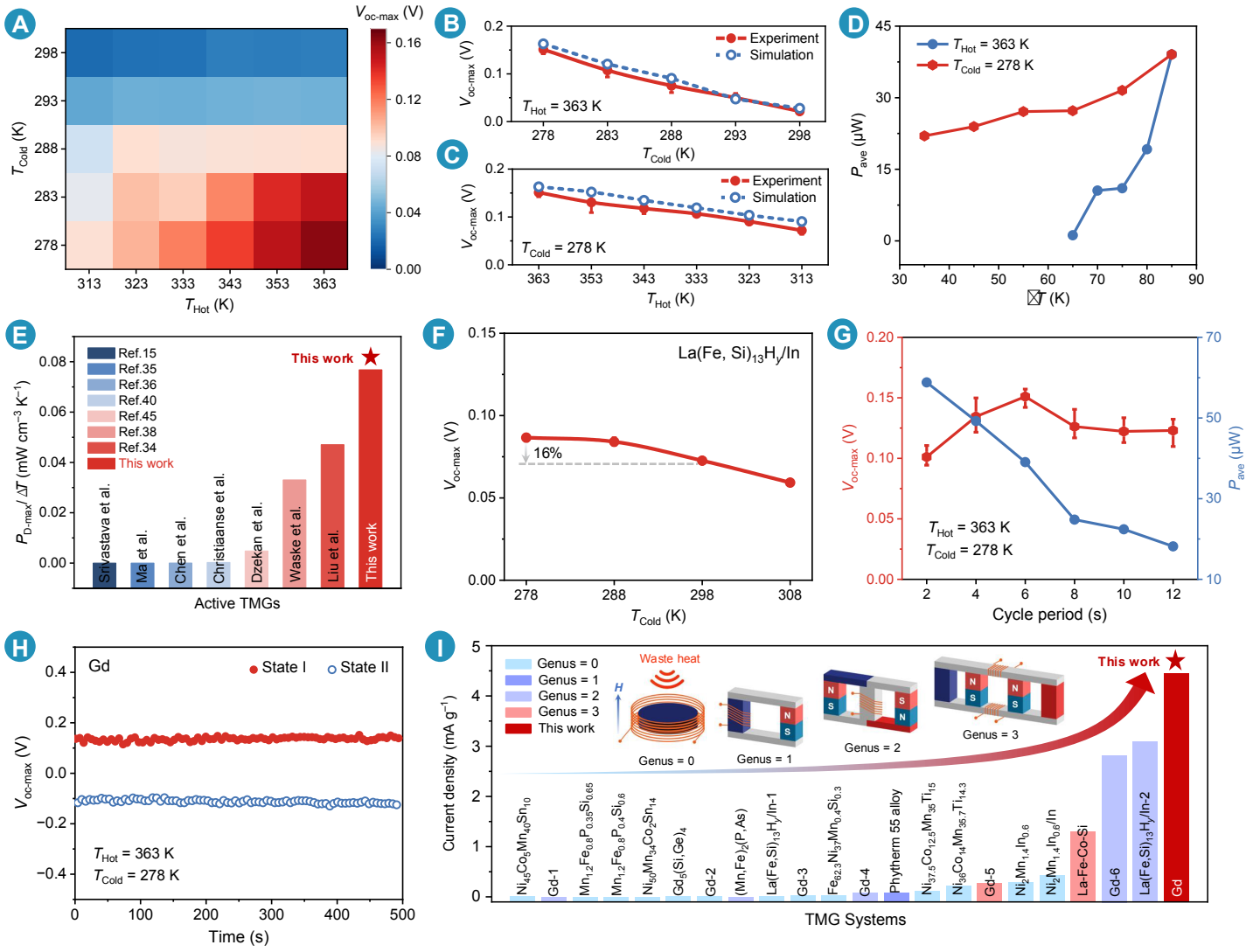


Figure 4. Measured and simulated peak voltage of the TMG depending on the key operating parameters (A) Simulated peak voltage as a function of cold source temperature (T_{Cold}) and hot source temperature (T_{Hot}). (B,C) Variation of peak voltage with T_{Cold} (B) and T_{Hot} (C) obtained from experiment and simulation. (D) The dependence of the average power on the temperature span (ΔT). (E) Comparison of normalized power density ($P_{D\text{-}max}/\Delta T$) between this work and reported active TMGs.[15,34-36,38,40,45] (F) Variation of peak voltage with T_{Cold} for La(Fe, Si)$_{13}$H$_y$/In composite. (G) Dependence of $V_{oc\text{-}max}$ and P_{ave} on cycle period. (H) Cycling stability of the TMG system over approximately 83 heating-cooling cycles for 500 s. (I) Summary of measured current density of conventional TMG materials based on different active TMG systems.[15,16,33-36,38-47] For topology-based TMGs, the current density is normalized by the TMM mass in one magnetic branch (see Supplemental Note 5 for details).

switched TMGs (8 s),[34] corresponding to a ~25% increase in operating frequency. In TMGs, the cycle period is governed by the coupled heat-transfer dynamics of the entire system, including solid conduction, fluid convection, and thermal inertia, rather than solely by intrinsic material properties. Therefore, further reduction becomes increasingly difficult as the cycle time approaches the thermal equilibration limit. When the cycle period is further reduced below 6 s, $V_{oc\text{-}max}$ starts to decrease significantly due to incomplete magnetic transitions caused by the temperature lag between the Gd and the alternating water flows. Nevertheless, the overall average power continues to rise until 2 s because of the increased number of voltage peaks per unit time. These results indicate that a cycle period of 6 s provides an effective balance between complete magnetic transition and high operating frequency, enabling stable voltage output while achieving enhanced average power performance.

To evaluate the short-term cyclic stability of the TMG, continuous heating-cooling tests were performed for 500 s, corresponding to approximately 83 complete thermal cycles (6 s per cycle), as shown in Figure 4H. The induced voltage amplitude and waveform remain nearly unchanged throughout the test, maintaining peak voltages of 0.15 V (state I) and −0.12 V (state II) with a variation of less than 5%. Post-cycling characterization further shows no appreciable change in the material properties and no observable structural degradation of the device (Figure S25). These results demonstrate good output repeatability and structural stability over the tested cycling period. Nevertheless, substantially longer cycling tests are required to establish the long-term durability and practical service lifetime of the TMG. These results confirm that the TMG can operate continuously and reliably under cyclic conditions, satisfying a key requirement for waste heat recovery applications.

Figure 4I compares the short-circuit current density (I_{sc}) of our device with previously reported active TMG systems. The labels indicate the types of working materials employed in the corresponding TMG systems. The present TMG achieves the highest I_{sc} of 4.5 mA g^{-1}, surpassing earlier records by up to 6 orders of magnitude.[15,16,33-36,38-47] As illustrated in the inset, active TMGs can be categorized by magnetic topology: conventional circuits (Genus = 0, 1) and topology-optimized architectures (Genus = 2, 3). In Genus = 0, 1 systems, the magnetic flux through the coil only oscillates between zero and maximum value during thermal cycling. In contrast, Genus = 2, 3 configurations enable flux reversal within the coil, yielding larger ΔB. The detailed operational mechanism of these TMGs is provided in Figure S26. The optimized magnetic topology and efficient flux transfer enable the present TMG to achieve a highly competitive I_{sc} among reported active TMG systems, reaching approximately 1.5 times the highest previously reported topological counterparts (Genus = 2, 3), and up to 6 orders relative to conventional ones

(Genus = 0, 1). Notably, when compared with previously reported Gd-based TMG systems (denoted as Gd-6), the optimized device in this work delivers a 1.6-fold higher current density. These results highlight that the improved TMG performance arises primarily from magnetic circuit optimization and device architecture design, rather than from differences in intrinsic material properties, establishing a new benchmark for active TMG systems.

Scalable TMG array and potential applications

To experimentally demonstrate the scalability of the proposed TMG architecture, six identical TMG units were electrically connected in series and integrated along a short shared heat-transfer channel (Figure 5A). Under the laboratory testing conditions, the short fluid-flow path minimizes the temperature decay of the circulating fluid along the array, allowing the voltage-accumulation capability of multiple TMG units to be evaluated without substantial variation in the thermal conditions among individual units. Each unit was designed with identical geometry and operated under the same thermal conditions to ensure uniform behavior. Alternating hot and cold water streams were circulated through the array, causing the electrical outputs from individual units to be superimposed, thereby proportionally amplifying the total voltage of the array. Multiple TMG units share the same heat-transfer channel, allowing the thermal energy carried by the heat exchange fluid to be harvested sequentially, thereby improving the overall efficiency of waste heat recovery. As shown in Figure 5B and Figure S27, the array delivers a maximum accumulated V_{oc} of ~0.8 V, nearly six times that of a single TMG unit, indicating a linear voltage scaling with the number of connected modules. Such linearity confirms the reproducibility of each unit and minimal electrical or magnetic interference between neighboring modules. These results verify that the induced voltage can be flexibly tuned by adjusting the array configuration.

Beyond this laboratory-scale demonstration, we further considered a more realistic waste heat recovery scenario involving temperature decay along an extended heat-transfer pipeline. During practical heat transport, the temperature of waste heat gradually decreases along the pipeline because of thermal losses, for example from about 363 K at the inlet to ~323 K at the outlet. A TMG array incorporating TMMs with graded T_Cs can therefore be arranged along the flow direction to match the local temperature distribution. Importantly, TMMs with substantially different T_C values are not intended to operate under an identical thermal window, as this could lead to incomplete magnetic switching and inefficient magnetic flux modulation. Instead, the operating temperature window of each TMG unit should sufficiently span the magnetic transition region of the corresponding TMM, thereby enabling a pronounced magnetization change during thermal cycling. As illustrated in Figure 5C, TMG units with higher T_C (e.g. 350 K) are positioned near the hot inlet, while those with lower T_C (e.g. 290 K) are placed downstream where the temperature is reduced. In this configuration, high-temperature heat is captured by high-T_C materials, and the remaining lower-temperature heat is subsequently utilized by low-T_C materials. Therefore, rather than requiring a universal temperature gradient for all TMMs, the optimal operating condition is determined by a T_C-matched thermal window for each material. Such temperature-matched operation broadens the effective working window and thereby improves overall utilization of low-grade waste heat.

To validate this concept, we compared Gd (T_C = 290 K) and a La(Fe, Si)$_{13}$H$_y$/In (T_C = 335 K) using the same TMG device. Figure 5D shows the voltage of Gd and La(Fe, Si)$_{13}$H$_y$/In at different T_{Cold} and T_{Hot}. Under identical conditions (T_{Hot} = 363 K, T_{Cold} = 278 K), both materials produced comparable voltages. When the T_{Hot} was reduced from 363 K to 323 K to simulate heat dissipation along the pipeline, the $V_{oc\text{-}max}$ of the La(Fe, Si)$_{13}$H$_y$/In decreased significantly by 93% (Figures S28 & S29), whereas Gd exhibited a smaller reduction of 40%, indicating that lower-T_C materials are more suitable for lower-temperature regions. Conversely, when the T_{Cold} increased from 278 K to 298 K, mimicking degraded cooling conditions, the $V_{oc\text{-}max}$ of Gd dropped sharply by 86%, while the La(Fe, Si)$_{13}$H$_y$/In showed only a 16% reduction, demonstrating the superior tolerance of higher-T_C materials at elevated operating temperatures. These contrasting responses demonstrate the importance of matching the operating thermal window to the T_C of the selected TMMs. Accordingly, materials with different T_C values exhibit complementary operating windows, and their integration into a graded-T_C TMG array provides a promising strategy for harvesting low-grade waste heat over a broad temperature range.

As a promising technology for harvesting low-grade waste heat, the output electricity of the TMG array could drive many Internet of Things (IoT) devices. Figure 5E shows the evolution of total output voltage and power as the number of TMG units in the array increases. A single module produces a $V_{oc\text{-}max}$ of ~0.15 V and an output power of ~24 μW, whereas six serially connected units deliver ~0.8 V and ~159 μW. The inset further illustrates the practical relevance of these outputs by mapping representative power levels to potential application domains:[50,51] single-module outputs fall within the range required for ultra-low-power sensors (e.g., RFID tag, pressure sensors), while the six-unit array approaches the operational threshold of compact wireless transmitters (e.g., hearing aid). Extrapolating the experimentally observed linear scaling trend indicates that a 30-unit array could provide ~6 V and ~1 mW, sufficient for devices such as miniature FM receivers and other low-power IoT nodes. The shared hot-water conduit and serial array configuration enhance overall thermal utilization: each additional module increases the portion of traversed waste heat converted into electricity without compromising individual unit performance. Compared with alternative low-grade waste heat harvesters such as miniature thermoelectric generators, the TMG array achieves milliwatt-level outputs through simple electrical stacking and a minimal material footprint, without requiring large thermal gradients or complex thermal management.[52] At the present proof-of-concept stage, the TMG is not intended to replace batteries in all compact IoT devices; rather, it is more appropriately viewed as a supplementary power source for scenarios with continuously available waste heat, where reduced battery replacement or recharging is desirable. Further miniaturization, integration, and cost reduction will be required for practical deployment in lightweight IoT systems. Furthermore, the modular nature of the TMG architecture enables cost reductions as the system scales, since both material and fabrication expenses can be significantly lowered through batch production. Overall, the scalability of the TMG array not only increases achievable output voltage and power, but also improves the cost-performance ratio, highlighting its strong potential for large-scale implementation in industrial low-grade waste heat recovery.

Moreover, in order to eliminate discrepancies from non-intrinsic factors and enable a fair performance comparison among different TMGs, we calculated the Power Generation Index (*PGI*), which incorporates both material and device parameters as $PGI = I_0/R\omega\Delta TH$, where ω is the coil winding number and H is the magnetic field.[16,36] As summarized in Table S2 and Figure 5F, our TMG attains the highest *PGI* of 6.8 among all reported active TMGs. In contrast, conventional designs (Genus = 0, 1) typically yield *PGI* values below 1.2, and topological systems (Genus = 2, 3) range from 10^{-4} to 6.2. Collectively, these results highlight the well-balanced combination of high output, thermal adaptability, and cycling stability achieved by our device. The synergistic optimization of heat transfer and magnetic flux coupling enables large dB/dt and rapid magnetic transitions, ensuring efficient and durable low-grade waste-heat harvesting. Such outstanding normalized performance, combined with the demonstrated linear scalability of the TMG array, underscores its strong potential for practical deployment in low-grade waste heat recovery and autonomous power supply applications.

CONCLUSION

In summary, we have developed a topology-optimized thermomagnetic generator that overcomes the long-standing limitations of stray-field leakage and incomplete flux utilization in existing TMGs. By integrating a compact magnetic circuit with strategically positioned, low-volume thermomagnetic elements, the device simultaneously accelerates heat exchange and maximizes the effective magnetic-flux variation. Quantitative analysis shows that 65.2% of the material-intrinsic flux change is transferred to the induction coil, substantially higher than the ~50–54% reported for pretzel-like and magnetocaloric-switch designs, resulting in significantly enhanced $d\Phi/dt$ and electrical output. Owing to this strengthened flux confinement and rapid thermal response, the generator achieves an open-circuit voltage density of 0.051 V g^{-1} and a power density of 5.76 mW cm^{-3}. In addition, the cycle period is reduced to 6 s, corresponding to a ~25% increase in operating frequency compared with earlier designs (~8 s), while maintaining stable and complete

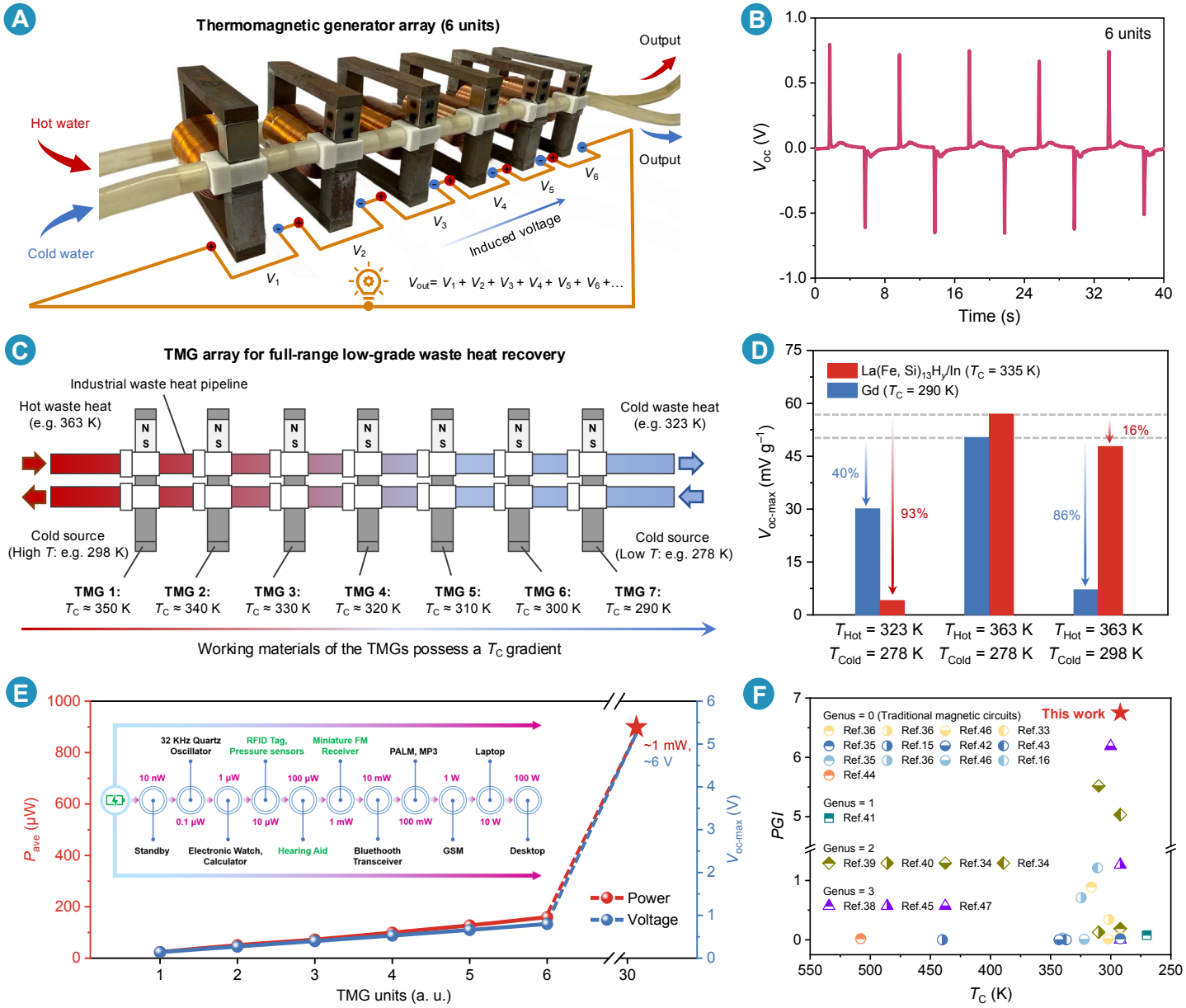


Figure 5. Scalable TMG array and potential practical applications (A) Photograph of the 6-unit TMG array electrically connected in series. (B) Measured V_{oc}–t curve of the 6-unit TMG array. (C) Schematic of the cascaded TMGs using working materials with a T_C gradient for full-range low-grade waste heat recovery. (D) The voltage of Gd and La(Fe, Si)$_{13}$H$_y$/In composite at different T_{Cold} and T_{Hot}. (E) Dependence of P_{ave} and $V_{oc\text{-}max}$ on the number of TMG units. The inset compares the achievable power range with the energy requirements of representative low-power electronic devices. (F) Comparison of the power-generation index (*PGI*) of this work with reported TMG systems of different magnetic circuit designs, including traditional magnetic circuits (Genus = 0) and topological-structure magnetic circuits (Genus = 1–3).

magnetic transitions within each cycle. The modular architecture further enables near-linear scaling of output, with a six-unit array producing approximately 0.8 V and 159 μW, demonstrating strong potential for distributed low-power energy harvesting and self-powered electronic systems. Notably, a TMG array constructed with TMMs possessing a graded T_C enables effective harvesting of waste heat over a broad temperature range, thereby significantly enhancing overall heat utilization efficiency. Importantly, by selecting TMMs with tailored Curie temperatures, the proposed device can operate under near-room-temperature cooling conditions, confirming its adaptability to practical thermal environments. Overall, this work demonstrates that magnetic topology optimization, combined with efficient thermal–magnetic coupling, provides a general and scalable strategy for significantly improving thermomagnetic energy conversion performance, offering new opportunities for low-grade waste heat recovery and autonomous energy systems.

REFERENCES

1. Schierning G. (2018). Bring on the heat. *Nat. Energy* **3**:92–93. DOI:10.1038/s41560-018-0093-4
2. Forman C., Muritala I.K., Pardemann R., et al. (2016). Estimating the global waste heat potential. *Renewable Sustainable Energy Rev.* **57**:1568–1579. DOI:10.1016/j.rser.2015.12.192
3. Straub A.P., Yip N.Y., Lin S., et al. (2016). Harvesting low-grade heat energy using thermo-osmotic vapour transport through nanoporous membranes. *Nat. Energy* **1**:1–6. DOI:10.1038/nenergy.2016.90
4. Firth A., Zhang B. and Yang, A. (2019). Quantification of global waste heat and its environmental effects. *Appl. Energy* **235**:1314–1334. DOI:10.1016/j.apenergy.2018.10.102
5. Hou, M. Chen H., Li S., et al. (2025). A tri-mode photothermal, phase-change, and radiative-cooling film for all-day thermoelectric generation. *Adv. Mater.* **37**:2505601. DOI:10.1002/adma.202505601
6. Wu G., Zhang Q., Tan X., et al. (2024). Bi_2Te_3-based thermoelectric modules for efficient and reliable low-grade heat recovery. *Adv. Mater.* **36**:2400285. DOI:10.1002/adma.202400285
7. Yan Q. and Kanatzidis M.G. (2021). High-performance thermoelectrics and challenges for practical devices. *Nat. Mater.* **21**:503–513. DOI:10.1038/s41563-021-01109-w
8. Shi X. and Chen L. (2016). Thermoelectric materials step up. *Nat. Mater.* **15**:691–692.

9. Bell L.E. (2008). Cooling, heating, generating power, and recovering waste heat with thermoelectric systems. *Science* **321**:1457–1461. DOI:10.1126/science.1158899
10. Shi X.-L., Zou J. and Chen Z.-G. (2020). Advanced thermoelectric design: From materials and structures to devices. *Chem. Rev.* **120**:7399–7515. DOI:10.1021/acs.chemrev.0c00026
11. Bu Z., Zhang X., Hu Y., et al. (2022). A record thermoelectric efficiency in tellurium-free modules for low-grade waste heat recovery. *Nat. Commun.* **13**:237. DOI:10.1038/s41467-021-27916-y
12. Ang A.K.R., Yamazaki I., Hirata K., et al. (2023). Development of $Cu_2Se/Ag_2(S,Se)$-based monolithic thermoelectric generators for low-grade waste heat energy harvesting. *ACS Appl. Mater. Interfaces* **15**:46962–46970. DOI:10.1021/acsami.3c09823
13. Li W., Goyal G.K., Stokes D., et al. (2023). High-performance skutterudite/half-Heusler cascaded thermoelectric module using the transient liquid phase sintering joining technique. *ACS Appl. Mater. Interfaces* **15**:2961–2970. DOI:10.1021/acsami.2c19137
14. Zhang Y., Li Z., Singh S., et al. (2023). Defect - engineering - stabilized $AgSbTe_2$ with high thermoelectric performance. *Adv. Mater.* **35**:2208994. DOI:10.1002/adma.202208994
15. Srivastava V., Song Y., Bhatti K., et al. (2011). The direct conversion of heat to electricity using multiferroic alloys. *Adv. Energy Mater.* **1**:97–104. DOI:10.1002/aenm.201000048
16. Chen H., Liu M., Yu Z., et al. (2025). Enhanced heat transfer for thermomagnetic generation in low-grade waste heat harvesting. *Adv. Mater.* **37**:2500544. DOI:10.1002/adma.202500544
17. Joseph J., Fontana E., Devillers T., et al. (2023). A Gd-film thermomagnetic generator in resonant self-actuation mode. *Adv. Funct. Mater.* **33**:2301250. DOI:10.1002/adfm.202301250
18. Gueltig M., Wendler F., Ossmer H., et al. (2017). High-performance thermomagnetic generators based on Heusler alloy films. *Adv. Energy Mater.* **7**:1601879. DOI:10.1002/aenm.201601879
19. Vuarnoz D., Kitanovski A., Gonin C., et al. (2012). Quantitative feasibility study of magnetocaloric energy conversion utilizing industrial waste heat. *Appl. Energy* **100**:229–237. DOI:10.1016/j.apenergy.2012.04.051
20. Deepak K., Varma V.B., Prasanna G., et al. (2019). Hybrid thermomagnetic oscillator for cooling and direct waste heat conversion to electricity. *Appl. Energy* **233-234**:312–320. DOI:10.1016/j.apenergy.2018.10.057.
21. Kishore R.A., Davis B., Greathouse J., et al. (2019). Energy scavenging from ultra-low temperature gradients. *Energy Environ. Sci.* **12**:1008–1018. DOI:10.1039/c8ee03084g
22. Kishore R.A. and Priya S. (2018). A review on design and performance of thermomagnetic devices. *Renewable Sustainable Energy Rev.* **81**:33–44. DOI:10.1016/j.rser.2017.07.035
23. Cugini F., Gallo L., Garulli G., et al. (2025). In-operando test of tunable Heusler alloys for thermomagnetic harvesting of low-grade waste heat. *Acta Mater.* **288**:120847. DOI:10.1016/j.actamat.2025.120847
24. Ahmed R., Kim Y., Mehmood M.U., et al. (2019). Power generation by a thermomagnetic engine by hybrid operation of an electromagnetic generator and a triboelectric nanogenerator. *Int. J. Energy Res.* **2**:2–11. DOI:10.1002/er.4691
25. Ujihara M., Carman G.P. and Lee D.G. (2007). Thermal energy harvesting device using ferromagnetic materials. *Appl. Phys. Lett.* **91**:093508. DOI:10.1063/1.2775096
26. Chun J., Kishore R.A., Kumar P., et al. (2018). Self-powered temperature-mapping sensors based on thermo-magneto-electric generator. *ACS Appl. Mater. Interfaces* **10**:10796–10803. DOI:10.1021/acsami.7b17686
27. Rodrigues C., Pires A., Gonçalves I., et al. (2022). Hybridizing triboelectric and thermomagnetic effects: A novel low-grade thermal energy harvesting technology. *Adv. Funct. Mater.* **32**:2110288. DOI:10.1002/adfm.202110288
28. Gong S., Wang X., Tang B., et al. (2024). Achieving self-reinforcing triboelectric-electromagnetic hybrid nanogenerator by magnetocaloric and magnetization effects of gadolinium. *Adv. Mater.* **36**:2402824. DOI:10.1002/adma.202402824
29. Lallart M., Yan L., Miki H., et al. (2021). Heusler alloy-based heat engine using pyroelectric conversion for small-scale thermal energy harvesting. *Appl. Energy* **288**:116617. DOI:10.1016/j.apenergy.2021.116617
30. Gueltig M., Ossmer H., Ohtsuka M., et al. (2014). High frequency thermal energy harvesting using magnetic shape memory films. *Adv. Energy Mater.* **4**:1400751. DOI:10.1002/aenm.201400751
31. Joseph J., Ohtsuka M., Miki H., et al. (2020). Upscaling of thermomagnetic generators based on Heusler alloy films. *Joule* **4**:2718–2732. DOI:10.1016/j.joule.2020.10.019
32. Joseph J., Ohtsuka M., Miki H., et al. (2022). Thermal processes of miniature thermomagnetic generators in resonant self-actuation mode. *iScience* **25**:104569. DOI:10.1016/j.isci.2022.104569
33. Liu X., Zhang H., Chen H. et al., (2023). Significant optimization of active thermomagnetic generator for low-grade waste heat recovery. *Appl. Therm. Eng.* **221**:119827. DOI:10.1016/j.applthermaleng.2022.119827
34. Liu X., Chen H., Huang J., et al. (2023). High-performance thermomagnetic generator controlled by a magnetocaloric switch. *Nat. Commun.* **14**:4811. DOI:10.1038/s41467-023-40634-x
35. Ma Z., Chen H., Liu X., et al. (2021). Thermomagnetic generation performance of Gd and $La(Fe, Si)_{13}H_y$/In material for low-grade waste heat recovery. *Adv. Sustainable Syst.* **5**:2000234. DOI:10.1002/adsu.202000234
36. Chen H., Liu X., Liu Y., et al. (2024). Excellent thermomagnetic power generation for harvesting waste heat via a second-order ferromagnetic transition. *Mater. Horiz.* **11**:2603–2614. DOI:10.1039/d3mh02225k
37. Chen H., Zhang H., Liu M., et al. (2026). High-performance thermomagnetic generation in low-grade waste heat recovery. *Chin. Phys. B* **35**:027201. DOI:10.1088/1674-1056/ae1205
38. Waske A., Dzekan D., Sellschopp K., et al. (2018). Energy harvesting near room temperature using a thermomagnetic generator with a pretzel-like magnetic flux topology. *Nat. Energy* **4**:68–74. DOI:10.1038/s41560-018-0306-x
39. Bahl C.R.H., Engelbrecht K., Gideon A., et al. (2024). Design, optimization and operation of a high power thermomagnetic harvester. *Appl. Energy* **376**:124304. DOI:10.1016/j.apenergy.2024.124304
40. Christiaanse T. and Brück E. (2014). Proof-of-concept static thermomagnetic generator experimental device. *Metall. Mater. Trans. E* **1**:36–40. DOI:10.1007/s40553-014-0006-9
41. Lallart M., Wang L., Sebald G., et al. (2014). Analysis of thermal energy harvesting using ferromagnetic materials. *Phys. Lett. A* **378**:3151–3154. DOI:10.1016/j.physleta.2014.09.016
42. Liu Z., Tegus O., Ou Z. et al., (2015). Thermomagnetic power generation of $Mn_{1.2}Fe_{0.8}P_{1-x}Si_x$ compounds in strongfield of permanent magnet. *Acta Phys. Sin.* **64**:047103. DOI:10.7498/aps.64.047103
43. Bi L., Tegus O., Yi R., et al. (2012). Thermomagnetic power generation performance of first-order phase transition material $Mn_{1.2}Fe_{0.8}P_{0.4}Si_{0.6}$. *Acta Phys. Sin.* **61**:077103. DOI:10.7498/aps.61.077103
44. Liu J., Long Y., Bai D., et al. (2019). Magnetic properties of FeNi alloys for high-temperature thermomagnetic power generation. *AIP Adv.* **9**:045227. DOI:10.1063/1.5086411
45. Dzekan D., Diestel A., Berger D., et al. (2021). Can gadolinium compete with La-Fe-Co-Si in a thermomagnetic generator. *Sci. Technol. Adv. Mater.* **22**:643–657. DOI:10.1080/14686996.2021.1957657
46. Chen H., Ma Z., Liu X., et al. (2022). Evaluation of thermomagnetic generation performance of classic magnetocaloric materials for harvesting low-grade waste heat. *Appl. Energy* **306**:117999. DOI:10.1016/j.apenergy.2021.117999
47. Jiang C., Zhu S., Yu G., et al. (2022). Numerical and experimental investigations on a regenerative static thermomagnetic generator for low-grade thermal energy recovery. *Appl. Energy* **311**:118585. DOI:10.1016/j.apenergy.2022.118585
48. Kishore R.A. and Priya S. (2018). A review on low-grade thermal energy harvesting: materials, methods and devices. *Materials* **11**:1081433. DOI:10.3390/ma11081433
49. Dzekan D., Waske A., Nielsch K., et al. (2021). Efficient and affordable thermomagnetic materials for harvesting low grade waste heat. *APL Mater.* **9**:011105. DOI:10.1063/5.0033970
50. Sarker M.R., Riaz A., Lipu M.S.H., et al. (2024). Micro energy harvesting for IoT platform: Review analysis toward future research opportunities. *Heliyon* **10**:e27778. DOI:10.1016/j.heliyon.2024.e27778
51. Haras M. and Skotnicki T. (2018). Thermoelectricity for IoT – A review. *Nano Energy* **54**:461–476. DOI:10.1016/j.nanoen.2018.10.013
52. He H., Wu Y., Niu C., et al. (2024). Toward tiny high-power-density thermoelectric harvesters. *Energy Convers. Manage.* **300**:117954. DOI:10.1016/j.enconman.2023.117954

FUNDING AND ACKNOWLEDGMENTS

This work was supported by the National Natural Science Foundation of China (Grant Nos.: 52671240, 52101210); the Fundamental Research Funds for the Central Universities (Grant No.: FRF-KST-26-012)； USTB Research Center for International People-to-people Exchange in Science, Technology and Civilization (Grant Nos.: 2024KFZD001 and 2024KFYB004).

AUTHOR CONTRIBUTIONS

H.Z. conceived the project. H.D.C. carried out the main experiments and wrote the original draft. H.D.C., M.Z.L. and S.Y.J. measured the TMG property. H.W.Z. prepared the TMG samples. H.N.L., J.Y.S. and K.M.Q. performed the magnetic measurements. D.D.W. and J.C.W. designed and built the circuit. Y.L.C., A.G.G. and S.V.T. discussed the results and reviewed the manuscript. H.D.C. and H.Z. prepared the manuscript with contributions from all authors.

DECLARATION OF INTERESTS

The authors declare no competing interests.

DATA AND MATERIALS AVAILABILITY

This study did not generate new unique materials.

SUPPLEMENTAL INFORMATION

It can be found online at https://doi.org/10.59717/j.xinn-energy.2026.100192